Chemical Science

ROYAL SOCIETY OF CHEMISTRY

EDGE ARTICLE

View Article Online
View Journal | View Issue

Cite this: *Chem. Sci.*, 2025, **16**, 17658

All publication charges for this article have been paid for by the Royal Society of Chemistry

Received 17th July 2025
Accepted 26th August 2025

DOI: 10.1039/d5sc05331e

rsc.li/chemical-science

A sequence-activated near-infrared fluorescence probe for precisely tracking *in vivo* senescence

Jiahuan Nong,[a] Pengcheng Li,[a] Mingming Zhu,*[b] Yifeng Li,[c] Changsheng Wang,[d] Yutao Zhang,[a] Chenxu Yan [a] and Zhiqian Guo *[ae]

Real-time monitoring of senescent cells is of great significance for understanding and intervening in aging. Since overexpression of endogenous β-galactosidase (β-gal) is not unique to senescent cells, probes relying solely on β-gal activity could yield inaccurate senescent cell detection. Herein, we designed a dual-mode sequential response AND logic NIR probe MFB-βgal, which contains a β-gal-cleavable unit and a morpholine unit, serving as an enzymatic activity trigger and a lysosomal targeting moiety, respectively. MFB-OH is generated *in situ* after reaction with β-gal, which can detect the alkalinization of lysosomes by emission intensity in senescent cells. This probe has been successfully used to distinguish between SKOV-3 and senescent cells and applied to *in vivo* visualization of β-gal activity in a mouse model, providing a new strategy for the accurate detection of cellular senescence.

Introduction

Cellular senescence is a state of irreversible cell-cycle arrest triggered by diverse stressors, including DNA damage, oxidative stress, and oncogenic activation.[1–5] It is a dynamic process that promotes the removal of abnormal cells by stopping proliferation, activating the immune system and secreting proinflammatory mediators.[6–9] The accumulation of senescent cells may lead to the sustained activation of the senescence-associated secretory phenotype, which is a trigger for organism dysfunction and age-related diseases such as fibrosis, neurodegeneration, and metabolic disorders.[8,10,11] Accurate and real-time monitoring of cellular senescence is essential for elucidating senescence-associated biological processes and developing targeted therapeutic strategies.[12–15] Conventional approaches such as SA-β-gal staining (X-gal-based) and western blotting remain the gold standards for senescent cell identification, yet they are technically demanding and inherently incompatible with live-cell or *in vivo* applications.[16–18] Fluorescent probes activated by β-galactosidase have emerged as powerful tools for *in vivo* imaging of senescence; however, their mere reliance on β-gal activity lacks sufficient specificity.[19–23] Notably, elevated β-gal activity is also observed in certain cancer cell lines (*e.g.*, SKOV-3 ovarian carcinoma), which may lead to false-positive results.[24–28] Therefore, these challenges underscore the development of next-generation probes that respond to multiple senescence-associated biomarkers, thereby enabling accurate and selective detection of senescent cells within complex biological environments.

Alongside the well-documented upregulation of β-galactosidase activity, senescent cells exhibit distinct alterations in the lysosomal microenvironment.[29–32] As a weakly acidic organelle, lysosomes maintain an acidic pH ranging from 4.5 to 5.0 under normal conditions.[33–37] This pH gradient is primarily regulated by a V-type ATPase (V-ATPase), which drives the transport of protons into the lysosomal lumen through the energy of ATP hydrolysis.[38–40] Based on these facts, we propose a multiparameter strategy to markedly enhance detection specificity.[41–43] By harnessing both β-galactosidase (β-gal) activity and lysosomal pH alkalinization as orthogonal triggers, we aim to construct a multiplexed optical probe capable of operating in living cells.[44] This design strategy necessitates two key features of the probe:[45] (i) accurate lysosomal targeting and (ii) the ability to simultaneously respond to both β-gal and pH through dual activation mechanisms. Inspired by the Boolean logic idea,[46–49] we envision integrating these two hallmark features of senescence as dual-input signals. Notably, achieving both organelle-specific targeting and logic-based responsiveness within a single molecular framework remains a formidable challenge. By implementing a sequential AND logic gate design, this system would deliver a highly specific output that reliably identifies senescent cells.

[a]*Shanghai Key Laboratory of Functional Materials Chemistry, Institute of Fine Chemicals, Frontiers Science Center for Materiobiology and Dynamic Chemistry, School of Chemistry and Molecular Engineering, East China University of Science and Technology, Shanghai 200237, China. E-mail: guozq@ecust.edu.cn*

[b]*Division of Gastroenterology and Hepatology, NHC Key Laboratory of Digestive Diseases, Shanghai Institute of Digestive Disease, Inflammatory Bowel Disease Research Center, Renji Hospital, School of Medicine, Shanghai Jiao Tong University, Shanghai, China. E-mail: gzqzmm@163.com*

[c]*No. 2 High School of East China Normal University, Shanghai 201203, China*

[d]*Department of Infection, Renji Hospital, School of Medicine, Shanghai Jiao Tong University, Shanghai, China*

[e]*State Key Laboratory of Bioreactor Engineering, East China University of Science and Technology, Shanghai 200237, China*

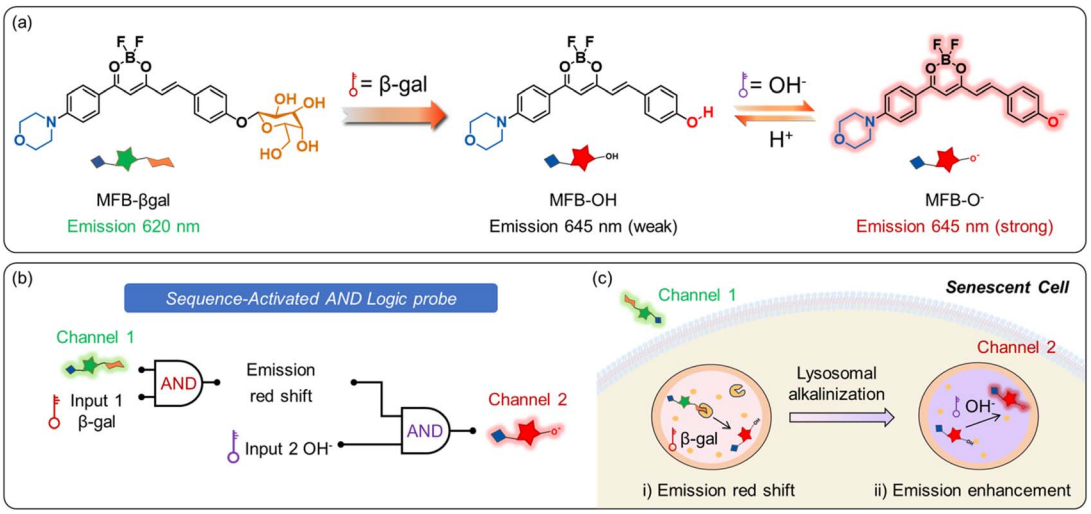

Fig. 1 Dual-channel sequence-responsive AND logic NIR fluorescent probe. (a) Chemical structure of MFB-βgal and the proposed sensing mechanism for aging. (b) Logic circuit diagram of the sequence-responsive AND logic nanoprobe for precise tracking of senescence *via* a dual NIR channel. (c) Schematic illustration of the sequential response process of MFB-βgal targeting senescent cells.

Herein, we present a sequence-responsive, AND logic-based dual-channel NIR fluorescent probe that functions as a programmable sensor for precise tracking of cellular senescence (Fig. 1). The scaffold BF2bdk was chosen due to its bilateral modifiability, enabling two essential functionalization:[50–54] (i) incorporation of a morpholine unit that serves as both a lysosome-targeting unit and an electron-donating group for extending the emission into the NIR region[55] and (ii) implementation of sequential responses for β-galactosidase activity and lysosomal pH sensing. Specifically, MFB-βgal is initially localized to the lysosome, where β-galactosidase cleaves the C–O glycosidic bond, *in situ* yielding the intermediate MFB-OH. Subsequently, due to its excellent pH sensitivity, it can respond to the elevated lysosomal pH associated with senescent cells. Critically, only upon the sequential triggering of both enzymatic and pH inputs does the probe exhibit a red-shifted emission accompanied by a pronounced fluorescence enhancement. By leveraging the probe's sequential dual-mode response to senescence-associated β-galactosidase (β-gal) activity and lysosomal alkalinization, the limitations of single-mode detection strategies have been effectively addressed. Moreover, MFB-βgal enables discrimination of cells at different stages of senescence and has been successfully applied for *in vivo* imaging of β-gal activity in tumour-bearing nude mice.

Results and discussion

We incorporated a lysosome-targeting group with β-gal/pH sequentially responsive moieties into a BF2bdk scaffold.[56] Morpholine exhibits a higher cumulative effect in lysosomes than in other organelles, demonstrating its effectiveness as a lysosomal targeting group.[57,58] MFB-βgal was effectively obtained through a classical Knoevenagel reaction, under neutral pH conditions. For details, please see the SI.

Enzyme-catalysed reaction and pH response test of MFB-βgal

First, the time-dependent change of fluorescence intensity was performed to verify the reaction kinetic profiles of MFB-βgal. As shown in Fig. S1, it takes ~27 min to reach a plateau, which is directly reflected by the fluorescence intensity at 645 nm. Upon excitation of the new absorption peak at 575 nm, the maximum emission at 645 nm was significantly enhanced, which depends linearly as a function of the β-gal concentration (from 0 U to 0.8 U) at a fixed incubation time with a detection limit of 3.4×10^{-4} U mL^{-1} (Fig. 2). To confirm that MFB-βgal can be hydrolysed in the presence of β-gal and generate MFB-OH *in situ*, HPLC and HRMS analyses were systematically performed. As shown in Fig. S4, the retention times of free MFB-βgal and MFB-OH are 5.2 and 6.0 min, respectively. After MFB-βgal reacting with 5 U β-gal, a new peak with a retention time of 6.7 min was observed, consistent with the retention time of free MFB-OH, indicating that MFB-βgal is the substrate of β-gal, and its hydrolysis product is MFB-OH. Furthermore, the cleavage product was further unambiguously confirmed by HRMS analysis. In the system where MFB-βgal was completely reacted with β-gal, a peak of the hydrolysis product MFB-OH was detected at *m*/*z* 398.1382 (Fig. S3). All these results confirm that the enzyme-catalysed reaction *in situ* produces MFB-OH.

After establishing MFB-OH as the enzymatic product, we further investigated its pH-responsive behaviour. As shown in Fig. 2c, the absorption of MFB-OH at 495 nm significantly decreased as the pH value increased from 3 to 10, while a new absorption peak gradually emerged at 575 nm. Accordingly, a significant enhancement in fluorescence intensity was observed as the pH increased, particularly the intensity showed an intensive increase when the pH was between 6 and 8 (Fig. 2d). However, in contrast to pH-sensitive MFB-OH, MFB-βgal is not significantly affected by changes in pH. These results indicate that MFB-βgal undergoes the first step of its sequential activation *via* enzymatic cleavage, generating MFB-OH *in situ*,

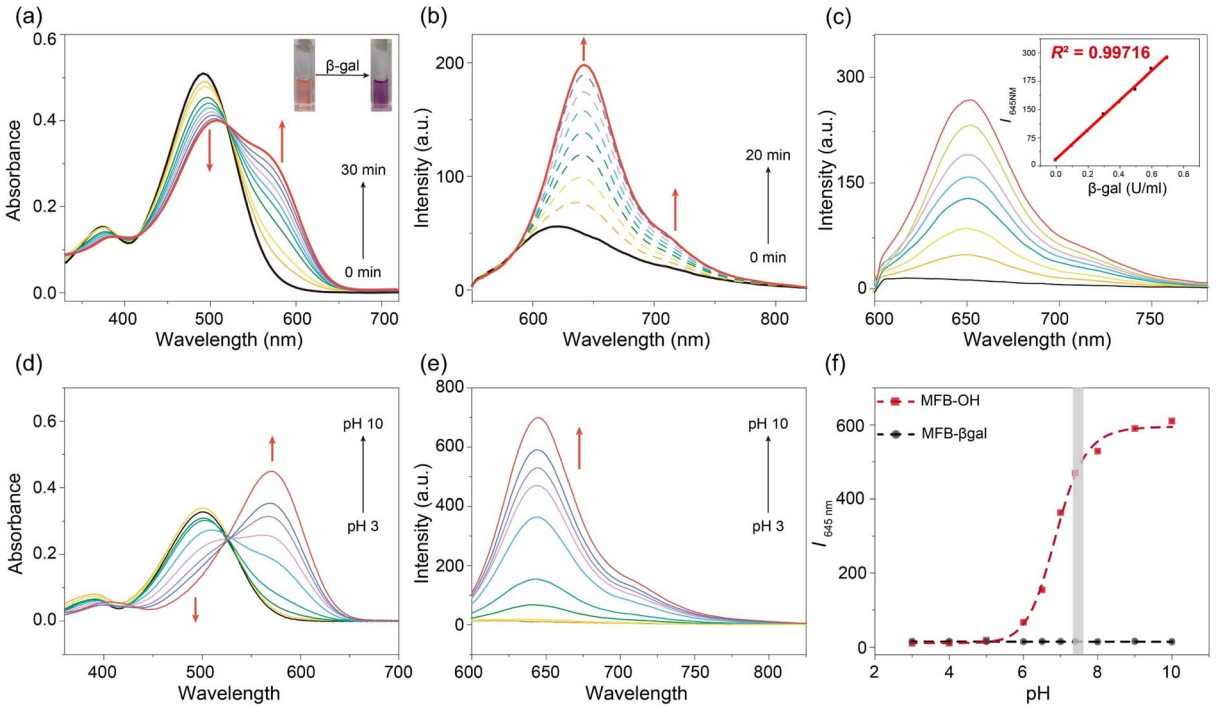

Fig. 2 Spectral profiles of MFB-βgal (10 μM) incubation with β-gal in a mixture solution (PBS/DMSO = 7 : 3, v:v; pH = 7.4) and pH properties of MFB-OH (10 μM). (a) Time dependence of absorption spectra (0–20 min). The inset shows the images before and after treatment with β-gal (2 U). (b) Time dependence of emission spectra (0–20 min), λ_{ex} = 525 nm. (c) Emission spectra of MFB-βgal upon incubation with β-gal (0–0.8 U), λ_{ex} = 575 nm. The inset shows the relationship between $I_{645\ nm}$ and β-gal concentration. (d) pH dependence of absorption spectra. (e) pH dependence of emission spectra. (f) pH dependence of $I_{645\ nm}$ in MFB-OH and MFB-βgal.

which subsequently enables the second step—pH sensing. Notably, elevated lysosomal pH has been widely recognized as a hallmark of cellular senescence. The enzymatic product MFB-OH exhibits excellent pH sensitivity, thereby completing the dual-step sequential response of MFB-βgal toward senescent cell detection.

Next, we carried out tests on the selectivity of MFB-βgal. To discriminate interferences from other biological analytes, the reactivity of MFB-βgal was examined against a variety of enzyme types, amino acids, inorganic salts and biomolecules. As shown in Fig. S5, a significant enhancement in the fluorescence signal at 645 nm (about 40-fold) was observed after incubation with β-galactosidase. However, a subtle change in fluorescence intensity was observed with the addition of other substances, indicating that the MFB-βgal probe has significantly higher selectivity for β-galactosidase than for other potential substances in biological systems.

Tracking endogenous β-gal activity *via* MFB-βgal

Encouraged by the desirable fluorescence response of MFB-βgal to β-gal, we further evaluated its use for tracking and imaging endogenous β-gal activity in live cells. First, the cytotoxicity of the probe was determined by MTT assay, as shown in Fig. S6. The results indicated that even after 24 hours of incubation with 20 μM MFB-βgal, the cell viability was as high as 95%, indicating that the probe exhibited negligible cytotoxicity to cells and could be used for live-cell imaging. Based on excellent biocompatibility and water solubility, the dual-channel cell imaging was investigated by confocal laser scanning microscopy (CLSM).

Subsequently, co-localization experiments were performed to study the lysosomal targeting ability of the probe MFB-βgal. In the experiment, we chose Lyso-Tracker Green, a commercially available lysosomal-targeting probe, because its emission spectrum avoids the emission region of MFB-βgal completely. As shown in Fig. 3a, SKOV-3 cells were incubated with Lyso-Tracker Green and then co-stained with MFB-βgal for 30 min. After comparing the signals in the green and red channels, Lyso-Tracker Green and MFB-βgal were found to have highly overlapping staining positions. Fluorescence co-localization analysis revealed that the overlap coefficient and Pearson coefficient of MFB-βgal were 0.9013 and 0.86 (Fig. S7), respectively. Co-localization experiments have shown that MFB-βgal exhibits good lysosomal targeting specificity, which lays the foundation for subsequent sequential response processes.

Based on the aforementioned experimental results, the imaging ability of the probe for endogenous β-gal in live cells was further investigated. The human ovarian cancer cell line SKOV-3 was chosen as a cell model due to its high endogenous β-gal levels, whereas human liver cancer cells (HepG2) were used as a control. As shown in Fig. 3, after incubating MFB-βgal (10 μM) with SKOV-3 cells for 30 min, fluorescence signals can be observed in both channels. It could be ascribed that SKOV-3 cells overexpressing endogenous β-gal resulted in enzymatic

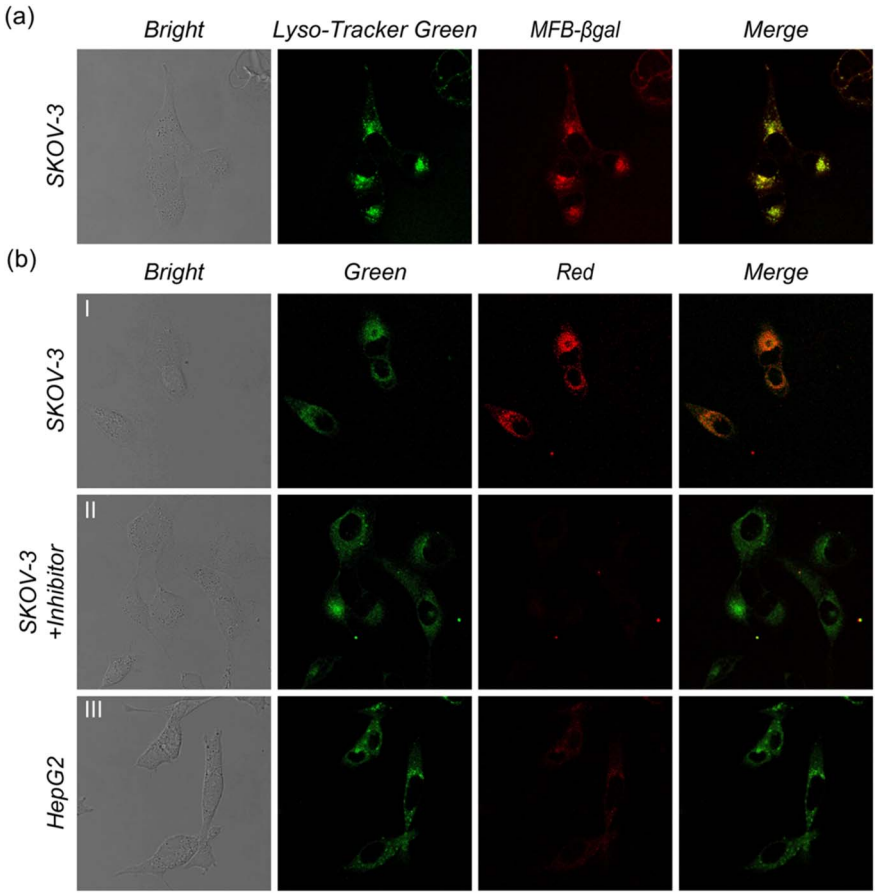

Fig. 3 CLSM images of endogenous glycosidases in lysosomes. (a) Colocalization imaging of MFB-βgal and Lyso-Tracker Green: SKOV-3 cells were incubated with MFB-βgal for 30 minutes, followed by co-staining with Lyso-Tracker Green for 30 min. (b) SKOV-3 and HepG2 cells incubated with MFB-βgal (10 μM) for 30 min: (I) SKOV-3 cells and (II) SKOV-3 cells pretreated with 1 mM inhibitor for 30 min and (III) HepG2 cells. Note: the green channel obtained from 560 to 620 nm, $\lambda_{ex} = 500$ nm; the red channel obtained from 650 to 800 nm, $\lambda_{ex} = 575$ nm.

cleavage of the probe, leading to the red-shift fluorescence emission. To verify that the fluorescent changes of the probe are indeed caused by endogenous β-galactosidase in cells, the SKOV-3 cells were incubated with D-galactose (β-galactosidase inhibitor) for 30 min to greatly reduce the amount of endogenous β-galactosidase. Under the inhibition of endogenous β-gal, MFB-βgal exhibited bright fluorescence in the green channel, while almost no fluorescence emission was observed in the red channel (Fig. 3b), illustrating that these obvious fluorescence changes were triggered by intracellular endogenous β-gal. Additionally, in the control group obtained after incubating with HepG2 cells, we also observed bright fluorescence signals in the green channel and very weak fluorescence in the red channel (Fig. 3b), suggesting that there is no overexpression of endogenous β-gal in HepG2 cells. After senescence induction, the fluorescence signal of the red channel was enhanced, indicating that the probe could respond to different senescence cells (Fig. S8 and S9). The results above confirm that MFB-βgal can image endogenous β-gal in live cells; at the same time, it marks the achievement of the first step of the sequential response.

Monitoring lysosomal pH change *via* MFB-βgal

After verifying the feasibility of the first trigger response, pH-responsive testing of the hydrolysis product MFB-OH was conducted. As is well-known, chloroquine has been demonstrated to be a drug capable of inducing lysosomal alkalinization, causing protons to leak from lysosomes and increasing lysosomal pH, and this process is similar to the cellular aging process. As shown in Fig. S10, compound MFB-OH was imaged with HepG2 cells pre-treated with different concentrations. It can be found that the fluorescence emission showed a relatively obvious enhancement with the addition of chloroquine, and the fluorescence intensity further increased with concentration. This result illustrates that the fluorescence intensity of MFB-OH gradually increases with the change in lysosomal pH, which also indicates the successful implementation of the second triggering process in the sequential reaction.

Differentiating senescent cells with β-gal overexpression

Based on the above conclusions, it was demonstrated that MFBs have the ability to respond to β-gal and pH, respectively. Thus, we adapted it for imaging and tracking senescent cells. It has been reported that lysosomes overexpress β-gal and are

accompanied by an increase in pH during the aging process of cells, which perfectly fits the process of sequential response. Different degrees of cellular aging models were constructed by incubating human renal proximal tubule epithelial cells (HK-2 cells) with doxorubicin for different days, which has been proven to induce cellular senescence.[59,60] To verify the successful construction of the aging model, we further compared the protein expression levels of aging biomarkers (P53, P21 and P16) in cells before and after induction. As expected, the results indicate the overexpression of the above aging markers in HK-2 cells induced by doxorubicin for 2 days (Fig. 4d). Based on the MFB-βgal reaction spectrum (Fig. 2b), we designated 540–600 nm as the green channel—its minimal fluorescence change pre- and post-reaction makes it an ideal internal reference. To selectively monitor the pH-dependent "turn-on" response, the red channel was confined to the 640–650 nm emission window. In this configuration, β-gal activity is signalled by the emergence of red-channel fluorescence, and subsequent lysosomal pH shifts are quantified by the ratio of red/green fluorescence-intensity, thus affording a sequential dual-mode response.

As shown in Fig. 4, in non-doxorubicin-treated HK-2 cells, only the green channel signal is observed, which is due to the absence of endogenous β-gal overexpression in normal HK-2 cells. Meanwhile, under the same conditions, the SKOV-3 cell model, which overexpress β-gal, displayed a weak fluorescence signal in the red channel. This is mainly ascribed to the inherent acidic lysosome of the SKOV-3 cells. After 24 h of doxorubicin treatment, HK-2 cells begin to show red-channel fluorescence, confirming β-gal activation in lysosomes. However, the overall red-channel fluorescence intensity remains weak and comparable to that of SKOV-3, indicating minimal lysosomal pH alkalization at this early senescence stage. Compared to the cells induced to age for 24 h, there was a remarkable increase in the red-channel intensity in cell induced for 2–4 days, consistent with progressive lysosomal pH elevation and enhanced fluorescence under weakly alkaline conditions. To further verify that this response arises from *in situ* – generated MFB-OH sensing of lysosomal pH changes, we tracked senescence with MFB-OH (Fig. S11). It can be observed that the control group exhibited red-channel weak fluorescence,

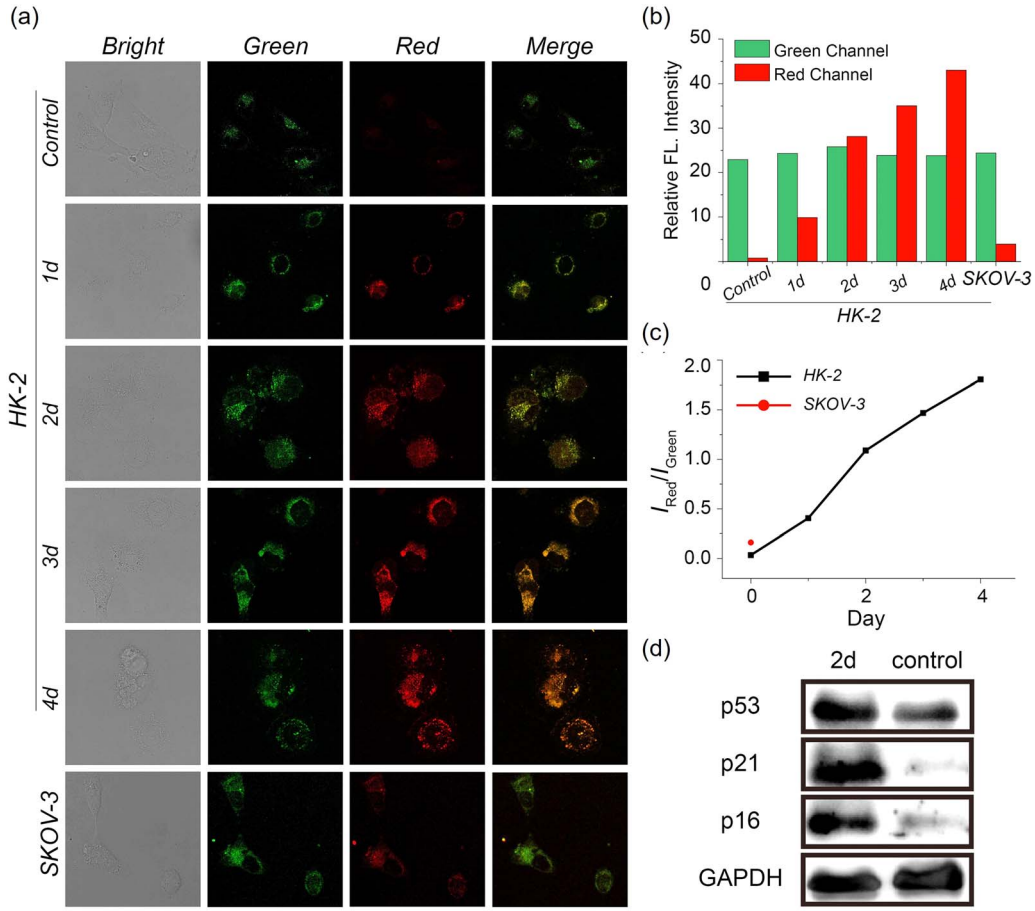

Fig. 4 Imaging of cellular senescence with probe MFB-βgal. (a) CLSM images of SKOV-3 cells and HK-2 cells at different aging levels. Row 1–5: Imaging of HK-2 cells treated without or with adriamycin (1 μM) for different times (1 day, 2 days, 3 days and 7 days) and then incubated with MFB-βgal (10 mM, 30 min). Row 6: Imaging of SKOV-3 cells incubated with MFB-βgal (10 mM, 30 min). Note: the green channel obtained from 540–600 nm, λ_{ex} = 525 nm; the red channel obtained from 640–650 nm, λ_{ex} = 575 nm. (b) Quantification of relative fluorescence intensity in the green channel and red channel of group (a). (c) Quantification of fluorescence intensity ratios (I_{red}/I_{green}) in group (a). (d) Western blot analysis to determine P53, P21 and P16 expressions in HK-2 cells treated without or with adriamycin (1 μM) for 2 days. GAPDH was used as an internal reference.

while a remarkable enhancement in fluorescence intensity confirming lysosomal alkalinization with advancing senescence. Together, these results demonstrate that MFB-βgal affords a sequential, dual-mode fluorescence response to β-gal expression and lysosomal pH changes during cellular aging.

Subsequently, a quantitative analysis was performed on the fluorescence intensity shown in Fig. 4b, reflecting changes in the intensity of green and red channel fluorescence over induction time. The green channel fluorescence intensity remained almost unchanged, while the red channel fluorescence intensity increased continuously. Therefore, the almost unchanged green channel can be used as a reference standard for measuring the fluorescence intensity of the red channel (R/G ratio), which improves the accuracy of cell senescence evaluation. In normal HK-2 cells, an extremely low R/G value (about 0.035) was observed, whereas the R/G value was enhanced 12-fold (about 0.41) after 1 day of doxorubicin induction. And the intensity continued to increase as the cells underwent further senescence, until the R/G value reached 1.80 after four days of induction, with a total 51-fold enhancement (Fig. 4c). However, a low R/G value (about 0.162) was also observed in SKOV-3 cells, which was extremely lower than that of senescent cells, enabling the probe to distinguish between SKOV-3 and truly senescent cells.

Benefiting from the design of dual-mode sequential response, MFB-βgal enables the precise detection of senescence, and the degree of cellular senescence can be reflected by the R/G ratio. A quantitative analysis of the fluorescence intensities (Fig. 4b) reveals that the green-channel signal remains essentially constant over the course of doxorubicin induction, whereas the red-channel intensity increases continuously. Consequently, the invariant green channel serves as an internal reference, and the red/green (R/G) fluorescence ratio provides a precise measure of senescence. In untreated HK-2 cells, the R/G ratio is very low (~0.035), increasing by ~12-fold to ~0.41 after 1 day of doxorubicin treatment. Continued induction leads to a progressive increase, with the R/G ratio reaching ~1.80 after 4 days – a total enhancement of ~51-fold (Fig. 4c). In contrast, β-gal–overexpressing SKOV-3 cells exhibit a modest R/G (~0.162), substantially lower than that of truly senescent cells, demonstrating the probe's ability to distinguish genuine senescence from mere β-gal overexpression. Thus, MFB-βgal's dual-mode, sequential fluorescence response enables both accurate detection and quantitative evaluation of cellular senescence.

Constructing a sequential AND logic gate for *in vivo* sensing of senescent cells

After summarizing the cell imaging results, a strong fluorescence signal in the red channel is produced only when both β-gal and lysosomal alkalization are present simultaneously. As such, an AND logic gate was built based on the programmable fluorescence response carried out by the two sequence-dependent inputs (Fig. 5). Specifically, β-gal and lysosomal alkalization were used as inputs, and the emission intensity at

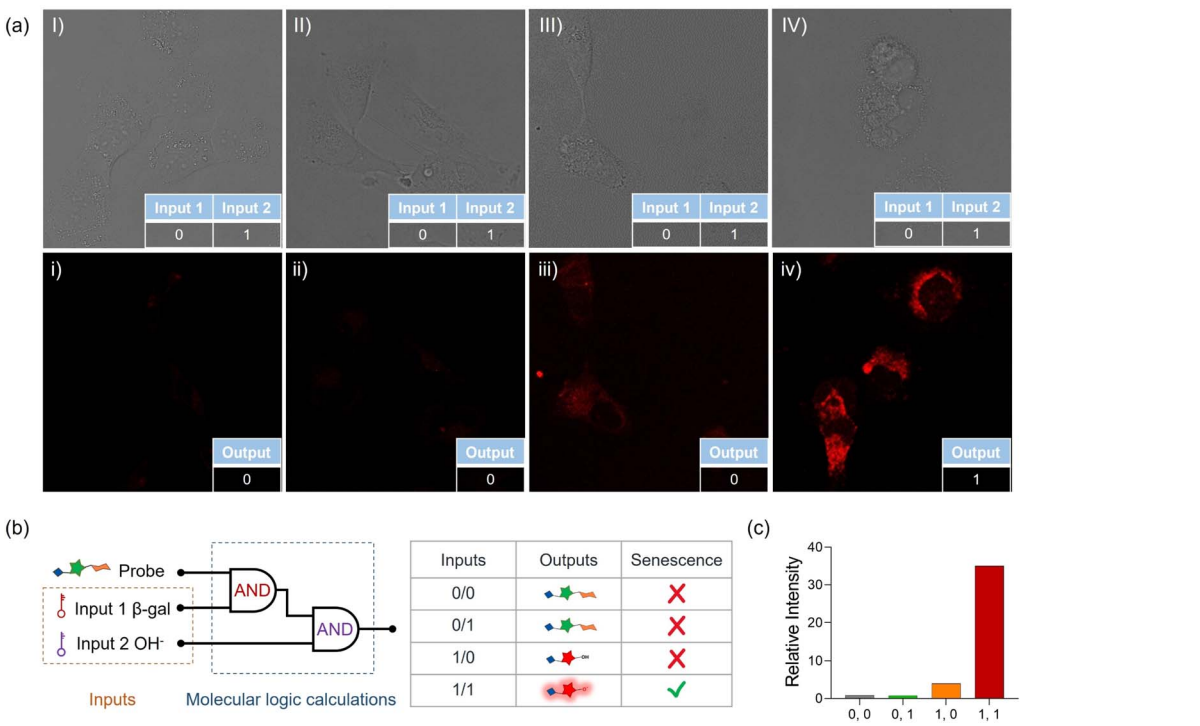

Fig. 5 Sequence-responsive AND logic behaviors of MFB-βgal. (a) Imaging results with MFB-βgal under different input signals: (I) and (i) A549 cells; (II) and (ii) A549 cells pretreated with chloroquine for 30 min; (III) and (iii) SKOV-3 cells; (IV) and (iv) HK-2 cells treated with adriamycin (1 μM) for 3 days. (b) Logic circuit diagram of the sequence-response and input/output result schematic. (c) Intensity of the output signal. Note: the red channel obtained from 640 to 650 nm, λ_{ex} = 575 nm.

645 nm (Red Channel) of the system served as the output. In terms of inputs, "1" and "0" denoted the presence and absence of β-gal and alkalization, respectively. For the output, fluorescence was characterized as "ON" and "OFF", which represented "1" and "0", respectively. Upon the presence of the dual inputs (1/1), an abrupt increase in fluorescence intensity took place, producing an output signal of "1". Taken all together, the success of the sequential AND logic gate, constructed based on the two senescence characteristics as inputs, provides a promising strategy for the accurate detection of aging.

Based on the NIR emission of MFB-βgal and its excellent intracellular imaging of β-gal, we were naturally lead to consider applying it to the real-time visualization of β-gal *in vivo*. A549 cells (without overexpressed β-gal) of the mouse model were utilized. The mouse model with overexpression of β-gal was established by pre-injecting β-gal into the tumour site, and then MFB-βgal was injected orthotopically (Fig. 6c and d). As a control, MFB-βgal was injected *in situ* after pre-injecting PBS into the nude mouse (Fig. 6a and b). Notably, the control group exhibits distinct fluorescence emission at the 600 nm channel, while a non-fluorescent signal is observed at the 730 nm channel (Fig. 6a and b). In contrast, for β-gal pre-injection at the tumour site of mice, a fluorescence signal at 730 nm was clearly observed in the tumour cells after only 5 min post-injection, indicating that MFB-βgal could be rapidly activated by β-gal *in vivo*. And the signal of the 730 nm channel continuously increases over time, reaching its maximum level after 2 h post-injection. The above results demonstrate that the probe MFB-βgal can be specifically activated by β-galactosidase, thereby enabling the visualization of β-galactosidase activity *in vivo*.

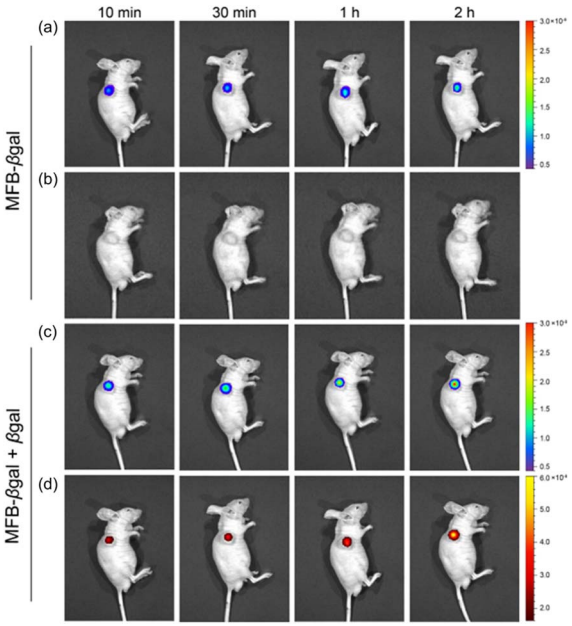

Fig. 6 Visualization of β-gal *in vivo*. Pre-treatment of the tumor site in tumor-bearing mice with PBS (a and b) or β-gal (c and d), followed by *in situ* injection of MFB-βgal (0.05 mg kg^{-1}). (a–d) Dual-channel fluorescence imaging of different time points (10 min, 30 min, 1 h and 2 h) after injection of MFB-βgal. Note: fluorescence signals at 600 nm (rainbow scale) and 730 nm (yellow-red scale).

Conclusions

In summary, we have developed a sequence-activated AND logic NIR fluorescence probe, MFB-βgal, to address the critical challenge of inaccurate *in vivo* senescence detection. The probe comprises a difluoroboron β-diketonate fluorophore, a β-galactosidase-responsive trigger, and a morpholine-based lysosomal targeting moiety, respectively. As expected, MFB-βgal is capable of imaging endogenous β-gal in living cells with an ultra-low detection limit (3.4×10^{-4} U mL^{-1}). Importantly, the enzymatic cleavage intermediate subsequently responds to lysosomal alkalization, allowing discrimination between SKOV-3 and senescent cells *via* emission intensity. Compared to previous methods, the utilization of the AND logic probe that takes the two features of aging as inputs significantly improves the accuracy of aging detection. Due to its NIR emission and excellent intracellular imaging of β-gal, it has also been applied to *in vivo* visualization of β-gal activity in a mouse model. Thus, this probe, based on the unique sequential-response AND logic design strategy, presents a robust strategy for precise detection and assessment of aging.

Ethical statement

This study was performed in strict accordance with the NIH guidelines for the care and use of laboratory animals (NIH Publication No. 85-23 Rev. 1985) and was approved by the Institutional Animal Care and Use Committee of National Tissue Engineering Center (Shanghai, China). The 4-week-old female BALB/c nude mice were produced from Shanghai Meixuan Biological Technology Co., Ltd, and maintained under standard conditions. The animals were housed in sterile cages within laminar airflow hoods in a specific pathogen-free room with a 12-h light/12-h dark schedule and fed autoclaved chow and water ad libitum. Ethical approval for the animal experiments was obtained prior to the research from the East China University of Science and Technology Animal Studies Committee, and the assigned approval number was ECUST-2021-07001.

Author contributions

All the experiments were conducted by J. N., P. L. and Y. L. under the supervision of Z. G., M. Z., C. W., C. Y. and Y. Z. participated in the article discussions. All authors discussed the results and co-wrote the manuscript.

Conflicts of interest

The authors declare no competing financial interest.

Data availability

All data generated and analyzed during the study are available from the corresponding authors upon reasonable request.

Supporting data have been included in the article's SI. See DOI: **https://doi.org/10.1039/d5sc05331e**.

Acknowledgements

This work was supported by NSFC/China (32394001, 22225805, 32121005, and 22378122), Shanghai Science and Technology Innovation Action Plan (No. 23J21901600), Shanghai Frontier Science Research Base of Optogenetic Techniques for Cell Metabolism (Shanghai Municipal Education Commission, grant 2021 Sci & Tech 03-28), Shanghai Pujiang Program (22PJ1411800), and Science and Technology Commission of Shanghai Municipality (24DX1400200).

Notes and references

1 R. Di Micco, V. Krizhanovsky, D. Baker and F. d'Adda di Fagagna, *Nat. Rev. Mol. Cell Biol.*, 2021, **22**, 75–95.
2 W. Huang, L. J. Hickson, A. Eirin, J. L. Kirkland and L. O. Lerman, *Nat. Rev. Nephrol.*, 2022, **18**, 611–627.
3 J. Campisi and F. d'Adda di Fagagna, *Nat. Rev. Mol. Cell Biol.*, 2007, **8**, 729–740.
4 V. Gorgoulis, P. D. Adams, A. Alimonti, D. C. Bennett, O. Bischof, C. Bishop, J. Campisi, M. Collado, K. Evangelou, G. Ferbeyre, J. Gil, E. Hara, V. Krizhanovsky, D. Jurk, A. B. Maier, M. Narita, L. Niedernhofer, J. F. Passos, P. D. Robbins, C. A. Schmitt, J. Sedivy, K. Vougas, T. von Zglinicki, D. Zhou, M. Serrano and M. Demaria, *Cell*, 2019, **179**, 813–827.
5 G. Kroemer, A. B. Maier, A. M. Cuervo, V. N. Gladyshev, L. Ferrucci, V. Gorbunova, B. K. Kennedy, T. A. Rando, A. Seluanov, F. Sierra, E. Verdin and C. López-Otín, *Cell*, 2025, **188**, 2043–2062.
6 J. M. van Deursen, *Nature*, 2014, **509**, 439–446.
7 A. Hernandez-Segura, J. Nehme and M. Demaria, *Trends Cell Biol.*, 2018, **28**, 436–453.
8 A. Kowald, J. F. Passos and T. B. L. Kirkwood, *Aging Cell*, 2020, **19**, e13270.
9 C. López-Otín, M. A. Blasco, L. Partridge, M. Serrano and G. Kroemer, *Cell*, 2023, **186**, 243–278.
10 B. Wang, J. Han, J. H. Elisseeff and M. Demaria, *Nat. Rev. Mol. Cell Biol.*, 2024, **25**, 958–978.
11 M. Collado and M. Serrano, *Nat. Rev. Cancer*, 2010, **10**, 51–57.
12 C. D. Wiley and J. Campisi, *Nat. Metab.*, 2021, **3**, 1290–1301.
13 J. Guo, X. Huang, L. Dou, M. Yan, T. Shen, W. Tang and J. Li, *Signal Transduction Targeted Ther.*, 2022, **7**, 391.
14 Y. Yao, S. Chen, C. Yan, J. Wang, J. Liu, W. H. Zhu, C. Fan and Z. Guo, *Angew. Chem., Int. Ed.*, 2024, **64**, e202416963.
15 Z. Li, J. Cheng, L. Huang, W. Li, Y. Zhao and W. Lin, *Anal. Chem.*, 2021, **93**, 13800–13806.
16 G. P. Dimri, X. Lee, G. Basile, M. Acosta, G. Scott, C. Roskelley, E. E. Medrano, M. Linskens, I. Rubelj and O. Pereira-Smith, *Proc. Natl. Acad. Sci. U. S. A.*, 1995, **92**, 9363–9367.
17 H.-L. Ou, R. Hoffmann, C. González-López, G. J. Doherty, J. E. Korkola and D. Muñoz-Espín, *Mol. Oncol.*, 2021, **15**, 2634–2671.
18 B. Uyar, D. Palmer, A. Kowald, H. Murua Escobar, I. Barrantes, S. Möller, A. Akalin and G. Fuellen, *Ageing Res. Rev.*, 2020, **64**, 101156.
19 Y. Yao, Y. Zhang, C. Yan, W.-H. Zhu and Z. Guo, *Chem. Sci.*, 2021, **12**, 9885–9894.
20 D. Asanuma, M. Sakabe, M. Kamiya, K. Yamamoto, J. Hiratake, M. Ogawa, N. Kosaka, P. L. Choyke, T. Nagano, H. Kobayashi and Y. Urano, *Nat. Commun.*, 2015, **6**, 6463.
21 B. Y. Lee, J. A. Han, J. S. Im, A. Morrone, K. Johung, E. C. Goodwin, W. J. Kleijer, D. DiMaio and E. S. Hwang, *Aging Cell*, 2006, **5**, 187–195.
22 N.-C. Yang and M.-L. Hu, *Exp. Gerontol.*, 2005, **40**, 813–819.
23 F. Wu, J. Liu, M. Tao, M. Wang, X. Ren and Z. Hai, *Anal. Chem.*, 2023, **95**, 10481–10485.
24 Q. Wu, Q.-H. Zhou, W. Li, T.-B. Ren, X.-B. Zhang and L. Yuan, *ACS Sens.*, 2022, **7**, 3829–3837.
25 I. Brusuker, J. M. Rhodes and R. Goldman, *J. Cell. Physiol.*, 2005, **112**, 385–390.
26 K. Gu, W. Qiu, Z. Guo, C. Yan, S. Zhu, D. Yao, P. Shi, H. Tian and W.-H. Zhu, *Chem. Sci.*, 2019, **10**, 398–405.
27 Q. Yu, L. Zhang, M. Jiang, L. Xiao, Y. Xiang, R. Wang, Z. Liu, R. Zhou, M. Yang, C. Li, M. Liu, X. Zhou and S. Chen, *Angew. Chem., Int. Ed.*, 2023, **62**, e202313137.
28 X. Luo, E. Hu, F. Deng, C. Zhang and Y. Xian, *Chem. Sci.*, 2025, **16**, 6507–6514.
29 J. Liu, W. Lu, D. Reigada, J. Nguyen, A. M. Laties and C. H. Mitchell, *Invest. Ophthalmol. Visual Sci.*, 2008, **49**, 772–780.
30 L. Wang, Y. Xiao, W. Tian and L. Deng, *J. Am. Chem. Soc.*, 2013, **135**, 2903–2906.
31 R. Gómez-Sintes, M. D. Ledesma and P. Boya, *Ageing Res. Rev.*, 2016, **32**, 150–168.
32 D. J. Kurz, S. Decary, Y. Hong and J. D. Erusalimsky, *J. Cell Sci.*, 2000, **113**, 3613–3622.
33 S. Ohkuma and B. Poole, *Proc. Natl. Acad. Sci. U. S. A.*, 1978, **75**, 3327–3331.
34 Q. Qiao, W. Yin, X. Wu, S. Wu, Y. Ruan, N. Xu, J. Li, Z.-S. Wu, X. Liu and Z. Xu, *Angew. Chem., Int. Ed.*, 2025, e202503916.
35 S. Ji, J. Li, X. Duan, J. Zhang, Y. Zhang, M. Song, S. Li, H. Chen and D. Ding, *Angew. Chem., Int. Ed.*, 2021, **60**, 26994–27004.
36 Y. Zhang, Z. Liu, N. Zhou, F. Guo, H. Guo, X. Chen, S. Qin, P. R. Chen and X. Fan, *Nat. Catal.*, 2025, **8**, 162–177.
37 W. Li, S. Yin, Y. Shen, H. Li, L. Yuan and X.-B. Zhang, *J. Am. Chem. Soc.*, 2023, **145**, 3736–3747.
38 K. Cotter, L. Stransky, C. McGuire and M. Forgac, *Trends Biochem. Sci.*, 2015, **40**, 611–622.
39 D. J. Colacurcio and R. A. Nixon, *Ageing Res. Rev.*, 2016, **32**, 75–88.
40 Y. Sun, M. Li, D. Zhao, X. Li, C. Yang and X. Wang, *eLife*, 2020, **9**, e55745.
41 L. Zhou, X. Zhang, Y. Dong, Y. Pan, J. Li, Y. Zang and X. Li, *ACS Sens.*, 2022, **7**, 1958–1966.
42 J. Tian, D. Shi, Y. Zhang, X. Li, X. Li, H. Teng, T. D. James, J. Li and Y. Guo, *Chem. Sci.*, 2021, **12**, 13483–13491.
43 J. Li, X. Zhao, Y. Zhang, Y. Lu, H. Xue, D. Li, Q. Liu, C. Yan, W. Chi, X. Xiao, W.-H. Zhu and Z. Guo, *Chem. Sci.*, 2025, **16**, 3228–3237.

44 Y. Gao, Y. Hu, Q. Liu, X. Li, X. Li, C.-Y. Kim, T. D. James, J. Li, X. Chen and Y. Guo, *Angew. Chem., Int. Ed.*, 2021, **60**, 10756–10765.
45 Y. Johmura, T. Yamanaka, S. Omori, T.-W. Wang, Y. Sugiura, M. Matsumoto, N. Suzuki, S. Kumamoto, K. Yamaguchi, S. Hatakeyama, T. Takami, R. Yamaguchi, E. Shimizu, K. Ikeda, N. Okahashi, R. Mikawa, M. Suematsu, M. Arita, M. Sugimoto, K. I. Nakayama, Y. Furukawa, S. Imoto and M. Nakanishi, *Science*, 2021, **371**, 265–270.
46 C. Yan, Z. Guo, Y. Liu, P. Shi, H. Tian and W.-H. Zhu, *Chem. Sci.*, 2018, **9**, 6176–6182.
47 S. Erbas-Cakmak, S. Kolemen, A. C. Sedgwick, T. Gunnlaugsson, T. D. James, J. Yoon and E. U. Akkaya, *Chem. Soc. Rev.*, 2018, **47**, 2228–2248.
48 J. Andréasson and U. Pischel, *Chem. Soc. Rev.*, 2010, **39**, 174–188.
49 C. Liu, S. Lu, C. Yan, X. Zhao, J. Yang, W. Zhang, X. Zhao, Y. Ge, X. You and Z. Guo, *Chem. Sci.*, 2025, **16**, 6837–6844.
50 M. Zhu, T. Wang, Y. Zhang, J. Nong and Z. Guo, *Sens. Actuators, B*, 2023, **391**, 134039.
51 B. Bai, C. Yan, Y. Zhang, Z. Guo and W.-H. Zhu, *Chem. Commun.*, 2018, **54**, 12393–12396.
52 G. Zhang, S. E. Kooi, J. N. Demas and C. L. Fraser, *Adv. Mater.*, 2008, **20**, 2099–2104.
53 X. Chen, G. Wang, J. Li, X. Chen, X. Zhao, Y. Zeng, Y. Su and K. Zhang, *Adv. Opt. Mater.*, 2024, **12**, 2301619.
54 J. An, K. Kim, H. J. Lim, H. Y. Kim, J. Shin, I. Park, I. Cho, H. Y. Kim, S. Kim, C. McLean, K. Y. Choi, Y. Kim, K. H. Lee and J. S. Kim, *Nat. Commun.*, 2024, **15**, 1004.
55 B. Feng, Y. Ma, F. Zheng, X. Huang, X. Feng, K. Zhang, L. Liu, F. Chen and W. Zeng, *Chem. Eng. J.*, 2023, **464**, 142554.
56 L. Shi, C. Yan, Y. Ma, T. Wang, Z. Guo and W.-H. Zhu, *Chem. Commun.*, 2019, **55**, 12308–12311.
57 H. Yu, Y. Xiao and L. Jin, *J. Am. Chem. Soc.*, 2012, **134**, 17486–17489.
58 N. A. M. Ligthart, M. A. R. de Geus, M. A. T. van de Plassche, D. Torres Garcia, M. M. E. Isendoorn, L. Reinalda, D. Ofman, T. van Leeuwen and S. I. van Kasteren, *J. Am. Chem. Soc.*, 2023, **145**, 12630–12640.
59 Y. Maejima, S. Adachi, H. Ito, K. Hirao and M. Isobe, *Aging Cell*, 2008, **7**, 125–136.
60 M. Karabicici, S. Alptekin, Z. Fırtına Karagonlar and E. Erdal, *Mol. Oncol.*, 2021, **15**, 2185–2202.